Biaxial testing of nanoscale films on compliant substrates: Fatigue and fracture

B. Erdem Alaca,[a] John C. Selby, M. T. A. Saif, and Huseyin Sehitoglu
Department of Mechanical and Industrial Engineering, University of Illinois, 1206 West Green Street, Urbana, Illinois 61801

(Received 6 November 2001; accepted for publication 6 May 2002)

Two problems of technological importance for microelectromechanical systems (MEMS) and microelectronics industry are addressed: fatigue of thin films and nanoscale film cracking. A device is described that can (1) conduct biaxial fatigue tests on thin films and (2) be utilized to study fracture patterns in nanoscale coatings under biaxial stress state. Thin-film specimens, in the form of circular membranes, are exposed to cyclic pressures between two fixed pressure limits. Corresponding pressure and specimen deflection are measured. Experimental results, including hysteresis loops spanning deflections of 15–50 μm are presented for 4.6-μm-thick polyimide films. Furthermore, the evolution of crack patterns in a 150-nm-thick Al film deposited on a polyimide substrate is studied. Critical mode I stress intensity factor for Al is extracted from experimental results. © *2002 American Institute of Physics.* [DOI: 10.1063/1.1488685]

I. INTRODUCTION

Evaluation of mechanical properties of thin films has attracted much attention due to the important role thin films play in microsensors, microactuators, and other microelectromechanical systems. Even though thin films are not always employed as structural elements, they are usually subject to various forms of loading. Hence, the reliability of these devices depends heavily on the performance of thin films. For example, stresses will develop in the thin film due to lattice mismatch (coherency stresses) or mismatch of thermal expansions (thermal stresses) between the thin film and its substrate.[1] Stresses, called intrinsic stresses, can also be generated during film growth due to various other mechanisms such as grain growth in the case of metallic films.[1–3]

The task of the measurement of mechanical properties of thin films is carried out using various experimental techniques. Uniaxial tensile testing, for example, is useful for the determination of elastic modulus and tensile strength, if accompanied by an accurate strain measurement.[4] Bulge testing is used to evaluate biaxial modulus of thin films and their residual stresses.[5] Although it recently became a popular testing method, its use dates back to early days of sheet metal and polymer testing.[6–8] Residual stress evaluation can also be achieved by substrate curvature measurements.[9] Yield strength, on the other hand, can be measured by indentation techniques.[10,11] However, none of the mentioned techniques addresses fatigue behavior of thin films, although mechanical or thermal cyclic effects can easily lead to fatigue failure.[12]

Reduction of residual stress as a function of thermal cycling was studied previously on thin films not released from the substrate,[13] where the evaluation of the fatigue behavior of the thin film itself is usually prevented by the existence of the substrate. On the other hand, the majority of fatigue studies on free-standing thin films employ cantilever-type specimens consisting of materials such as Ag (Ref. 14) or Ni–P.[15] This particular selection of specimen geometry usually eliminates certain materials, including polymers. Furthermore, the multiaxiality of fatigue, another important aspect, is neglected, although the stress state in a thin film (coherency, thermal, or intrinsic stresses) is usually biaxial. In addition to this, there are also applications, including micropumps,[16] where a free-standing thin film undergoes biaxial loading. Although uniaxial fatigue tests on thin films are conducted using commercial load frames with high-precision load cells, results cannot directly be transferred to engineering applications. To address these issues, the testing device of this article is designed to study the fatigue behavior of thin films under biaxial loading. Thin-film specimens are subjected to cyclic loading with a frequency range up to 50 Hz, and the resulting load-deflection data are recorded. Phenomena such as ratchetting can be monitored, and fatigue life studies can be conducted.

Another issue of paramount technological importance is the cracking of thin films and coatings. Depending on film, substrate, and interface properties, biaxial stresses in thin films will lead to various forms of failure, including film cracking, substrate spalling, and interface debond.[17] Various theoretical treatments of this problem are available.[17–19] Careful experiments can be conducted with the apparatus of this article to observe the evolution of crack patterns and relate them to the fracture toughness of the chosen material.

The remainder of the article explains the principles of operation of the apparatus. Specimen preparation will be discussed, and experimental results from monotonic, cyclic, and fracture studies will be presented.

II. EXPERIMENTAL SETUP

A. Main components

The testing apparatus of this article, shown in Fig. 1, resembles a bulge tester with additional capabilities of cyclic

[a]Electronic mail: alaca@uiuc.edu

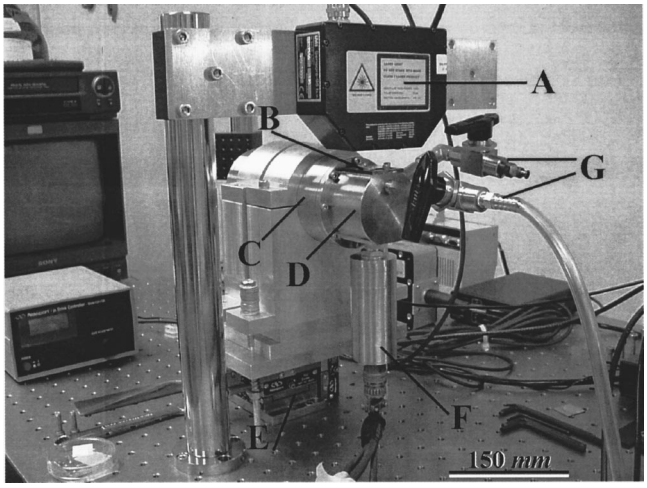

FIG. 1. Main components of the testing device. Thin-film specimen (B) is mounted on a fluid chamber (D), in which pressure is cycled with a chosen frequency by the motion of a piston driven by a piezoelectric actuator located in cylinder C. Corresponding displacements of the specimen are measured with a laser sensor (A), and a pressure transducer (F) is employed for pressure measurements. Two stainless-steel fittings (G) serve as inlet and bleeding valves for the fluid chamber. The setup is placed on a multiaxis translation stage (E).

loading, feedback control, and enhanced data acquisition. The main components, also designated in Fig. 1, include:

- Piezoelectric actuator: The particular piezoelectric actuator in this setup is a P-239.60 HVPZT translator by Physik Instrumente (PI) GmbH and Co. It has a 100 μm open-loop travel at the maximum operating voltage of 1000 V.
- Laser sensor: A 812330-SLS 7001/15 specular reflection laser sensor by LMI Selcom, Inc. with a measurement range of 1 mm and a resolution of 0.25 μm is used for displacement measurements at a fixed point, usually the midpoint, of the specimen. It produces a class II, 675 nm laser with a 10 μm spot size at a stand off of 15 mm. A camera is also incorporated within the sensor.
- Pressure transducer: Pressure measurements are carried out using a PX 951-100 S5V pressure transducer by OMEGA Engineering, Inc. with a range of 100 psi (0.6895 MPa) and an accuracy of $\pm 0.15\%$.

As shown schematically in Fig. 2, a piston is attached to the tip of the piezoelectric actuator, and the actuator is placed inside a stainless-steel cylinder. This assembly imparts the piston a travel of 100 μm. A separate chamber is attached to the end of the cylinder and filled with hydraulic oil, specifically, DTE 25 (registered trademark of Mobil Oil Corporation). With the piston resting on two O rings, the cylinder and the piezoelectric actuator are completely sealed off from the oil-filled chamber.

Prior to filling the chamber, the specimen is mounted on to the chamber via a specifically designed specimen holder, a steel plate with a circular hole in the middle. The specimen is a silicon wafer coated with a thin film of any desired thickness and composition. A window of any shape, usually circular, is micromachined in the silicon wafer exposing the thin film to the underlying oil. It is important that the chosen fluid is inert and does not alter the properties of the specimen. More on specimen preparation will be discussed later. The specimen is attached to the specimen holder using epoxy. The specimen holder is then screwed on to the testing device, where an O ring between the specimen holder and the testing device prevents any leakages. To prevent overloading of the specimen while mounting, the specimen holder is not screwed tightly at this stage. Details of the specimen and specimen–specimen holder assembly are shown in Fig. 3.

After the specimen is mounted, the setup is positioned vertically. As shown in Fig. 4, oil is pumped through a side fitting into the chamber while another fitting at the top of the chamber serves as a bleeding valve. This way of filling the chamber eliminates the possibility of having air bubbles trapped inside. The next step is the final tightening of the specimen holder. The fact that both valves are open at this

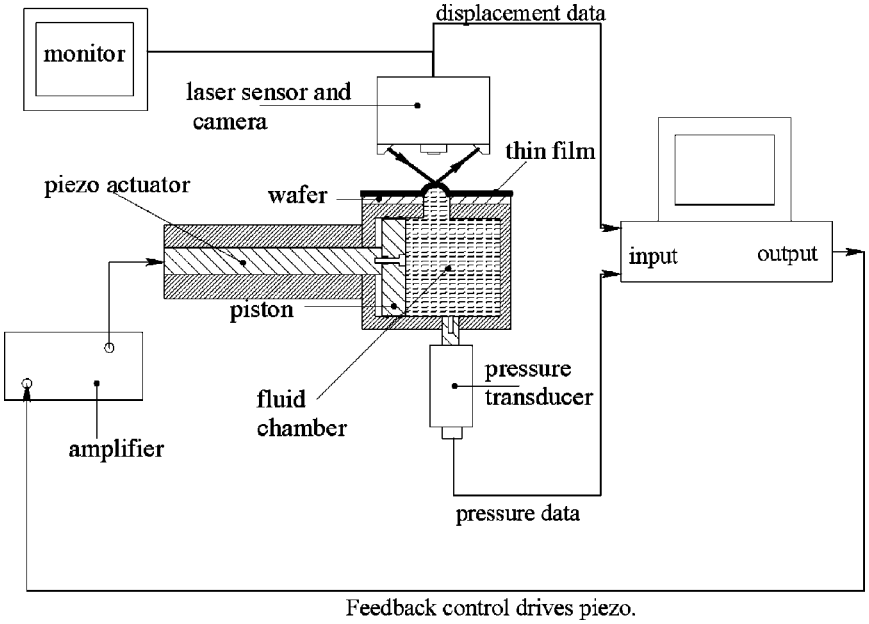

FIG. 2. Schematic of the setup showing details of (1) the actuator-piston-fluid chamber design, and (2) data flow in the control loop.

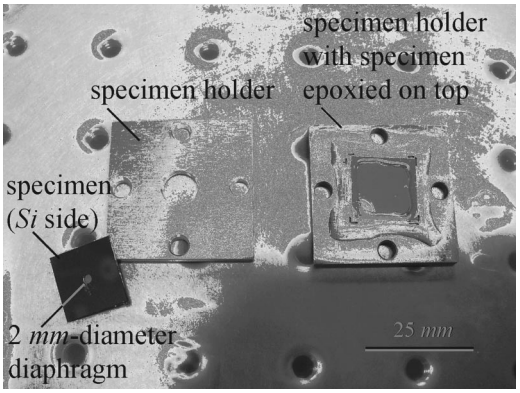

FIG. 3. Specimen consists of a thin film on a rectangular silicon die with a micromachined window at its center. Another hole is drilled at the center of the specimen holder, a rectangular metal plate. The specimen is epoxied on to the specimen holder, and the thin film is subjected to fluid pressure via the micromachined window. Here, the photograph shows (1) the silicon side of a specimen with a 2-mm-diam window, (2) a specimen holder with its central hole and four screw holes along the edges, and (3) a specimen epoxied to the specimen holder.

stage prevents any pressure buildup inside the chamber and, hence, the specimen is not overloaded. After the valves are closed, the setup is turned back to its horizontal position, which was shown in Fig. 1. Finally, the complete setup is mounted on a multiaxis translation stage with two micrometers controlling horizontal positioning and a piezoelectric actuator driving the setup vertically. This will facilitate specimen alignment with respect to the laser beam. The multiaxis stage is attached on top of a vibration isolation table. At the final stage, a few laser scans are conducted and the setup is tilted accordingly to ensure that the specimen is perfectly horizontal. Thereafter, the device is ready for operation.

B. Principles of operation

The operation of the setup is shown schematically in Fig. 2. The motion of the piezoelectric actuator displaces a certain volume of hydraulic oil via the attached piston. Since the fluid chamber was freed of air using the bleeding valve and since the walls of the cavity and the piston, made of steel, are relatively rigid entities, the displaced volume will be directly

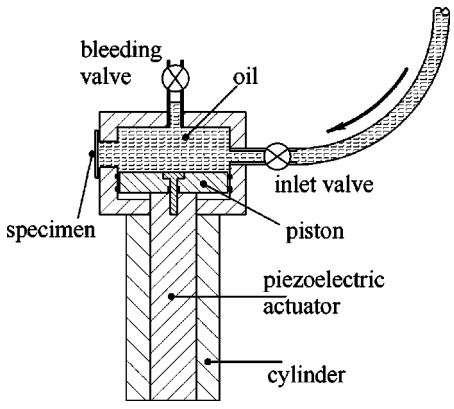

FIG. 4. Eliminating air from the hydraulics is crucial for the success of the device. It is achieved by feeding oil from a side fitting into the chamber, while a bleeding valve at the top allows trapped air to escape.

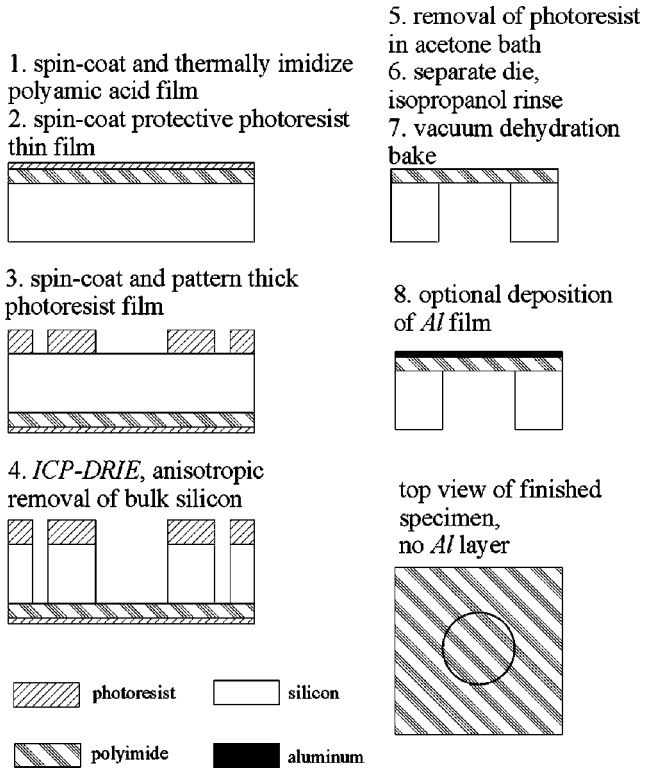

FIG. 5. Flow chart of the fabrication process.

accommodated by the deflection of the thin-film specimen, thereby raising pressure in the chamber.

As mentioned previously, measurements are taken by two main components:

- the laser sensor measuring midpoint deflection of the specimen bulging under pressure, and
- the pressure transducer measuring the pressure inside the oil chamber.

These two measurements serve as input to a closed-loop control program created by LabVIEW software (registered trademark of National Instruments). By driving the piston under feedback control, this program allows pressure to be cycled between two fixed limits with a chosen frequency and a wave shape. Having characterized the main components and the operation of the testing machine, the next sections will be devoted to specimen preparation and experimental results.

C. Specimen preparation

Specimens used for both biaxial fatigue and fracture studies consist of an aromatic polyimide diaphragm suspended on a bulk-micromachined silicon die. All polyimide diaphragms are derived from spin-coated and thermally imidized pyromellitic dianhydride 4,4 oxydianiline PMDA–ODA polyamic acid precursor films. For fracture experiments, an Al layer is deposited on the polyimide diaphragm. In the following section, specimen fabrication will be summarized. An accompanying chart can be found in Fig. 5.

A double-sided polished, p-doped, 1–3 Ω cm resistivity, n-type, $\langle 100 \rangle$ silicon wafer is the standard substrate for all samples. After cleaning the wafer in a modified SC-1 step of

the RCA clean process,[20] the wafer is baked at 180 °C for 15 min, and then spin coated with a commercially available aminosilane adhesion promoter. A bake of the adhesion promoter at 110 °C for 5 min is required, after which the wafer is spin coated with Pyralin PI-2808 (registered trademark of HD Micro Systems). Following a 15 min bake of the polyamic acid film at 60 °C in ambient air, thermal imidization is carried out in two steps at 240 °C for 2 h and at 350 °C for 4 h under a 200–500 mTorr pressure of dry nitrogen. Temperature ramps of approximately 1.5 °C/min are used between all temperature steps, including the initial heating from and final cooling to room temperature. Films spin coated and imidized from this process were 4.6 μm thick. After imidization is complete, a 2–3-μm-thick film of AZ 5214 (registered trademark) photoresist is spin coated on the polyimide and baked at 110 °C for 10 min in order to provide a protective coating to minimize surface damage incurred during subsequent processing steps.

Once polyimide processing is completed, the backside of the silicon wafer is coated with a 6–7-μm-thick AZ 4620 (registered trademark) photoresist film to serve as an etch mask for an inductively coupled plasma deep reactive ion etching (ICP-DRIE) process of the bulk silicon substrate.[21,22] The photoresist film is patterned such that a modified Bosch process[22] can be used to anisotropically etch through the bulk silicon (400–500 μm), sectioning the wafer into independent 15 mm by 15 mm square silicon die, each with a 2 or 6-mm-diam circular hole revealing the underlying polyimide film. The ICP-DRIE process of the silicon terminates once the polyimide film is exposed, resulting in a free-standing, suspended polyimide diaphragm. A Plasma-Therm, Inc., SLR Series Plasma Processing System is used for all ICP-DRIE processes.

After bulk micromachining of the silicon substrate, both photoresist masks are removed in an acetone bath, the individual die are then rinsed with isopropanol and subjected to a vacuum dehydration bake at 240 °C for 4–8 h to remove absorbed solvents. Once again, 1.5 °C/minute temperature ramps are used to both heat and cool the specimens. For fracture studies, a 150-nm-thick Al layer is sputtered on the surface of the polyimide immediately following the dehydration bake to prevent undue absorption of water from the ambient air in the polyimide film, providing a more experimentally reliable metal/polymer adhesive interface. Optional sputtering of Al thin films on the surface of the polyimide diaphragm for fracture studies is performed using a dc magnetron power supply at 300 W with an argon flow rate of 20 sccm and a chamber pressure of $2.3-2.8\times10^{-2}$ Torr.

Test specimens described here can also be used for studying interfacial failure between polymer thin films and silicon substrates.[23] However, it is noted that the pressures utilized in this study were not of a magnitude large enough to initiate interfacial delamination.

III. EXPERIMENTAL RESULTS

A. Monotonic response

Before demonstrating the capability of the apparatus to conduct fatigue testing, let us briefly discuss the monotonic response of the specimen. Figure 6 shows pressure versus midpoint deflection readings obtained on a 2-mm-diam specimen. Loading and unloading followed the same path in experiments indicating an elastic behavior. Finite-element studies have shown that the elastic response of a circular membrane under an applied pressure p can be approximated by the following formula:[9]

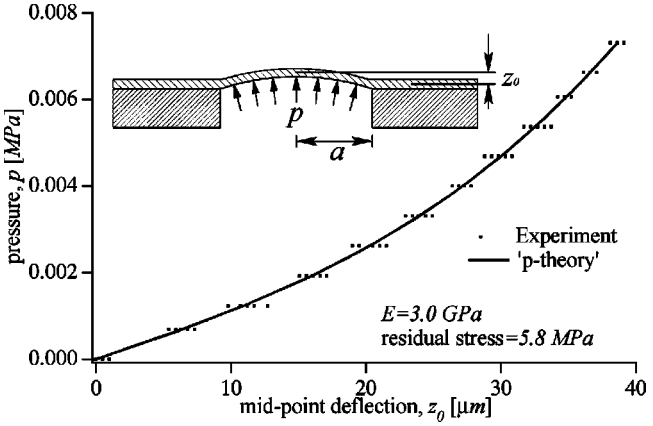

FIG. 6. Pressure vs midpoint deflection readings obtained on a 2-mm-diam specimen. Fitting the equation governing the elastic response of a circular plate to the experimental data, one obtains elastic modulus E and residual stress σ_0 of the thin film. Inset shows the bulging specimen with the laser pointing to its midpoint.

$$p=(1-0.24\nu)\left(\frac{8}{3}\right)\left(\frac{E}{1-\nu}\right)\left(\frac{h}{a^4}\right)z_0^3+4\left(\frac{\sigma_0 h}{a^2}\right)z_0, \qquad (1)$$

where E and ν are the elastic modulus and Poisson's ratio, respectively, h is the thickness and a is the radius of the thin film. z_0 is the midpoint deflection resulting from applied pressure p, and σ_0 is the residual stress. The membrane is clamped at its boundary. Fitting Eq. (1) to the experimental data, one can extract quantities such as elastic modulus E of the thin film and residual stress σ_0 for a given Poisson's ratio. In our case, the elastic modulus is found to be 3.0 GPa, and residual stress is 5.8 MPa for $\nu=0.4$. These results are in close agreement with previously reported PMDA-ODA properties.[24]

For the determination of actual stresses, on the other hand, further consideration is required. A major drawback of bulge testing is the usually indirect way of relating pressure and displacement data to the actual stresses and strains in the material. Employing a series solution to the equations of equilibrium, stresses in a circular membrane with clamped edges under a uniform, lateral loading were first calculated by Hencky[25] for large deflections. His analysis was later modified for the case of true pressure by Fichter.[26] A mechanistic discussion of the problem can be found in Ref. 16. Hencky's analysis was also modified for the existence of residual stresses by Campbell.[27] Campbell's study shows how coefficients of the series solution can be determined from equilibrium equations and clamped boundary condition for a chosen Poisson's ratio. This method is adopted here and results for various Poisson's ratios are shown in Fig. 7, where equibiaxial stress σ at the midpoint is given as a function of residual stress σ_0. Hence, once the residual stress is

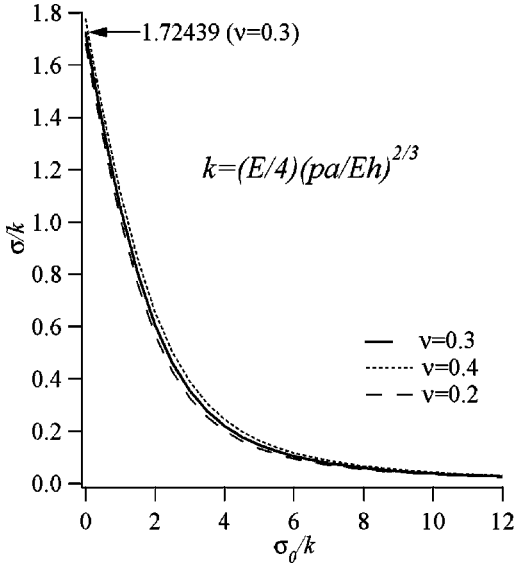

FIG. 7. Equibiaxial stress σ at the midpoint plotted against residual stress σ_0 for different Poisson's ratios. The dependence on Poisson's ratio is rather weak. $\sigma+\sigma_0$ is the total stress. Once σ_0 and E are determined experimentally, σ can be extracted from this figure for a given pressure p. The solution procedure by Campbell (Ref. 27) is summarized in the Appendix.

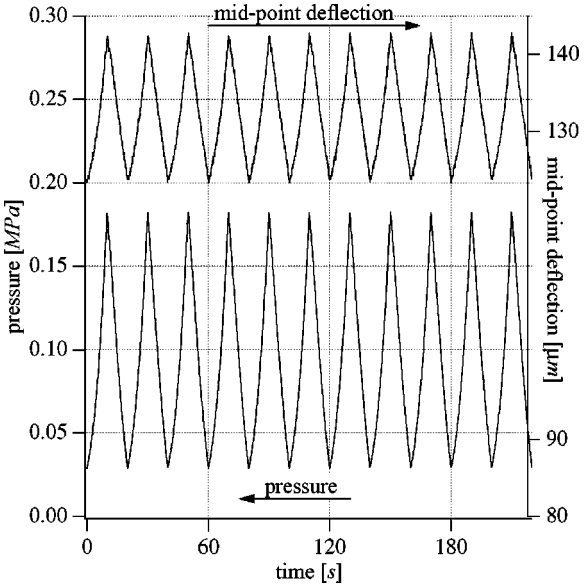

FIG. 9. Pressure history from a test where a 2-mm-diam specimen is subjected to pressure-controlled cyclic loading with a frequency of 0.05 Hz. Pressure is cycled between 0.029 and 0.182 MPa. The corresponding history of midpoint deflection is plotted above.

determined from Fig. 6, σ can be extracted from Fig. 7, and $\sigma+\sigma_0$ will be the total stress at the midpoint. Utilizing this method, strains at the midpoint are calculated for two different sets of specimens with 2- and 6-mm-diam diaphragms and the results are presented in Fig. 8. Generally overlooked, this method proves to be concise and straightforward. The main steps of the solution procedure for stresses are summarized in the Appendix. The interested reader is also referred to Campbell's work[27] for an in-depth study on the effect of residual tension on midpoint deflection. This was also utilized here to verify the fitting function given by Eq. (1) and a close correspondence is obtained.

Our discussion has hitherto been limited to linear elastic behavior. A similar correlation between applied pressure and actual stresses in the material needs to be established for plasticity, which requires additional theoretical work. This is also necessary for any modeling effort that addresses fatigue-related damage mechanisms. The next section deals with the results of fatigue experiments that were conducted with the testing device of this article.

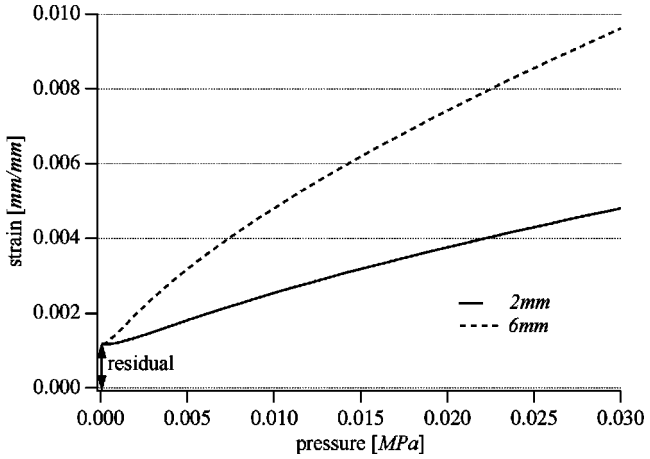

FIG. 8. Variation of strains at the midpoint of 2- and 6-mm-diam specimens as a function of applied pressure. Calculation of strains is carried out by utilizing σ_0 and E of Fig. 6 in Campbell's method (Ref. 27) summarized in Fig. 7. The initial offset is an indication of the existence of residual stress.

B. Fatigue testing

Figure 9 shows the pressure and deflection history from a test where a 2-mm-diam specimen was subjected to a pressure-controlled cyclic loading between 0.029 and 0.182 MPa with a frequency of 0.05 Hz. Cycles 100–110 are shown in Fig. 9 with the time axis chosen arbitrarily to start at zero.

Depending on the specimen dimensions, a wide range of deflections and pressures can be measured. Using a 6-mm-diam specimen, the hysteresis loops shown in Fig. 10 are obtained. They span a range of 50 μm at relatively low pressures with a frequency of 0.05 Hz. When the diameter of the specimen is decreased to 2 mm, deflections become smaller accordingly, and hysteresis loops spanning deflections as small as 15.7 μm, shown in Fig. 11, can be captured with the current setup. Demonstrating the capability of the testing apparatus to resolve small deflections and pressures, Figs. 10 and 11 do not necessarily convey information about the actual material behavior of polyimide because a single specimen was used for multiple tests. However, one phenomenon is evident in each figure: cyclic creep or ratchetting. In each cycle, a certain amount of plastic strain accumulates in the direction of the mean stress, which is also observed in uniaxial fatigue tests of polyimide.

C. Thin-film fracture under biaxial stress state

The reliability of multilayers is usually determined by geometry, materials mismatch, and interface quality. In the case of stiff coatings, fracture and delamination are common reasons of failure. This issue can also be addressed under the

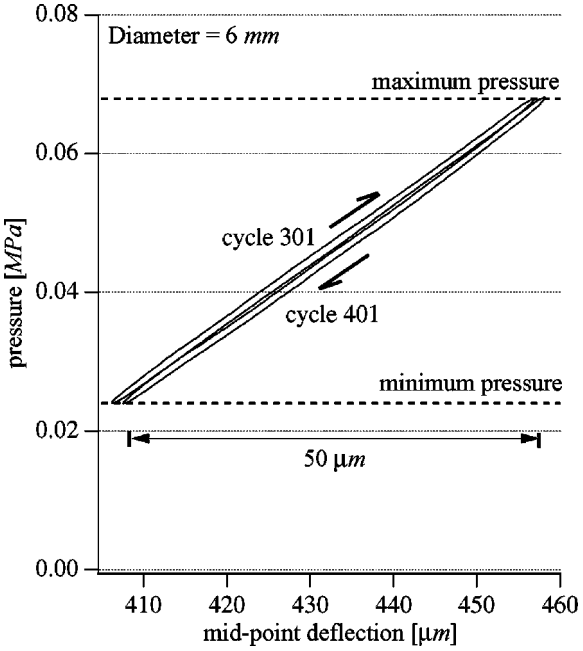

FIG. 10. Hysteresis loops obtained by using a 6-mm-diam specimen. Midpoint deflection spans a range of approximately 50 μm at relatively low pressure levels (0.024–0.068 MPa) with a frequency of 0.05 Hz. Ratchetting is evident.

biaxial stress state using the present apparatus. Polymeric membranes with a thin metallic layer deposited on top will be used. Replacing the laser sensor with a microscope, one can observe the behavior of the metallic coating while the pressure is increased. Since a curved surface is to be observed, the diameter of the specimen should be small, and lens magnification should be chosen as high as possible. Due

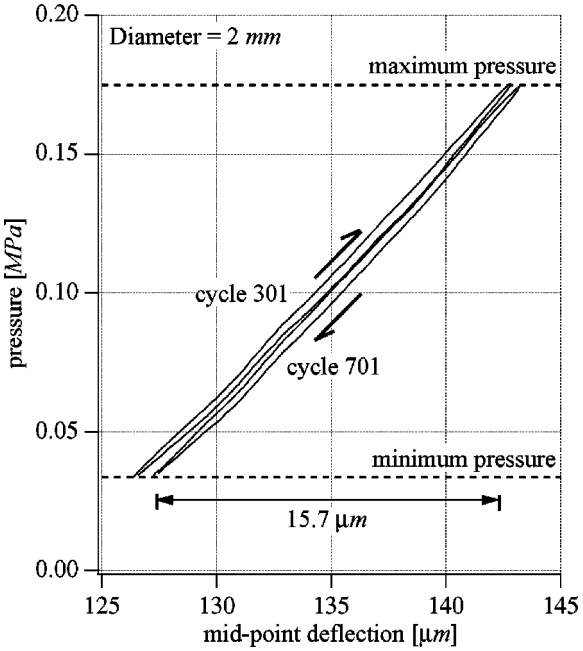

FIG. 11. Wide range of hysteresis loops can be captured with the testing apparatus. Choosing a smaller specimen size (2 mm diam) leads to smaller deflections even at higher pressures compared to the results given in Fig. 10. Here, hysteresis loops from the test of Fig. 9 are given spanning a displacement range of 15.7 μm. Ratchetting is evident again.

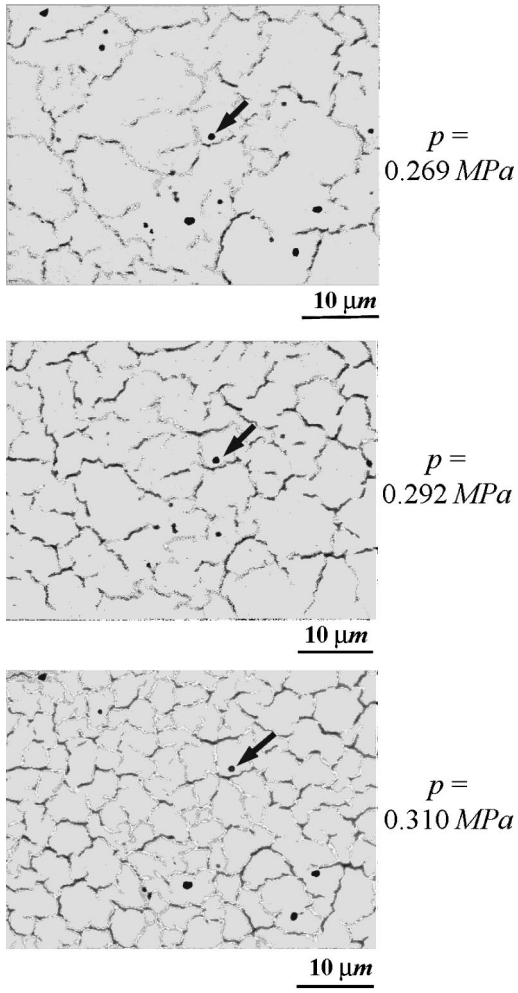

FIG. 12. Micrographs from an *in situ* test showing the evolution of the fracture pattern in a 150-nm-thick Al layer on a 4.6-μm-thick polyimide substrate as a function of the applied pressure. The observed area is very close to the midpoint of the 2-mm-diam specimen.

to the fact that the apparatus is placed on a vibration isolation table and the possibility of remote focusing via the piezoelectric actuator driving the stage vertically, high-magnification lenses can be used without difficulty, and *in situ* microscopy can be conducted with sharp focus.

The micrographs in Fig. 12 show the evolution of the fracture pattern in a 150-nm-thick Al layer on a 4.6-μm-thick polyimide substrate as a function of the applied pressure. The observed area is very close to the midpoint of the specimen. The network of cracks continues to develop until the specimen delaminates from silicon die at a pressure of 0.324 MPa. A detailed view of the fracture pattern is given in Fig. 13. The same type of cracking was previously reported in much larger length scales in a variety of environments where the biaxial stress state is present, for example, ceramic coatings on steel substrates,[28] drying coffee–water mixture,[29] or starch–water mixture,[30] on a glass plate or volcanic rocks,[31] and desiccating muds and clays.[32–34]

The first stage of crack formation involves independent, straight cracks channeling in the film with no interactions in between. It has been shown by Beuth[18] that if the film is stiffer than the substrate, the crack will propagate all the way to the interface in the thickness direction, given that the criti-

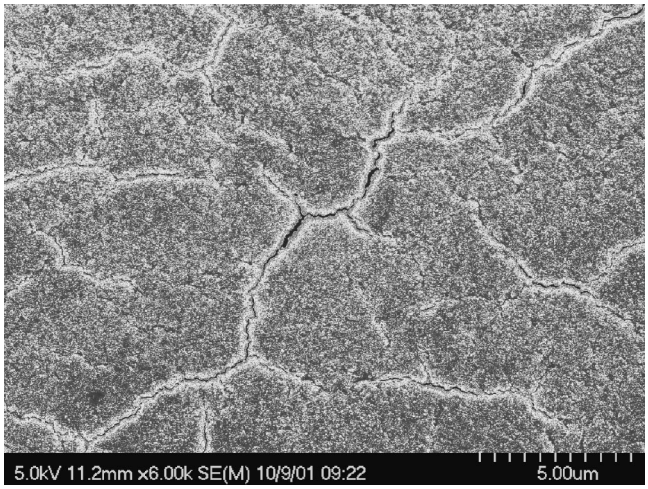

FIG. 13. Scanning electron micrograph of the Al surface of a 2-mm-diam specimen (150 nm Al/4.6 μm polyimide) showing details of the fracture pattern.

cal stress intensity factor is reached. The channeling front, on the other hand, will assume a steady-state shape after the crack length in the plane of the film exceeds several film thicknesses.[17] The energy release rate G associated with this steady-state propagation of an isolated crack has been calculated by Beuth.[18] Equating G to the mode I fracture toughness of the film will provide the condition for the propagation of the crack, because energy release rates of short cracks are lower than this steady-state value.[19] Once activated, these cracks will propagate, start interacting with each other, and ultimately form crack networks similar to those given in Fig. 12. Assuming that the crack arrests at the interface without penetrating into the substrate, G is given by[18]

$$G=\frac{1}{2}\frac{(1-\nu_f^2)h\sigma^2}{E_f}\pi g(\alpha,\beta), \tag{2}$$

where $g(\alpha,\beta)$ is a nondimensionalized integral of crack opening displacement defined and tabulated in Ref. 18 with α and β being the two Dundur's parameters characterizing the elastic mismatch. E_f and ν_f are the elastic modulus and Poisson's ratio of the film, respectively. σ is the biaxial stress state with one axis perpendicular to the crack line.

In our experiments, steady-state channeling was observed to take place at $p=0.235$ MPa when the cracks were straight and isolated. Assuming that the Al coating is too thin to interfere with the deformation of the polymeric substrate, the midpoint deflection of the membrane was calculated from Eq. (1) to be 157.9 μm. Since the Al coating conforms to the shape of the polymeric substrate, the equivalent pressure at which the metallic coating would take this imposed shape is calculated in the absence of residual stresses using Hencky's work[25]

$$z_0=0.653a\sqrt[3]{\frac{pa}{E_f h}}. \tag{3}$$

This equivalent pressure is plugged into Hencky's[25] stress formula to find the corresponding biaxial stress σ at the midpoint,

$$\sigma=0.431\sqrt[3]{E_f p^2\frac{a^2}{h^2}}, \tag{4}$$

which is then plugged into Eq. (2) to calculate G, where $g(\alpha,\beta)$ for the Al–polyimide case is taken from Ref. 18. G, which at the same time is the critical mode I fracture toughness, is found to be 5.96×10^{-5} MPa m. Finally, using the plane stress relation

$$G=\frac{K_I^2}{E}, \tag{5}$$

the critical mode I stress intensity factor K_I^c for the 150-nm-thick Al coating is obtained:

$$K_I^c=2.04\ \text{MPa}\sqrt{\text{m}}. \tag{6}$$

ACKNOWLEDGMENTS

This work was funded by DARPA under Contract No. DABT63-97-C-0069. The authors gratefully acknowledge help from Jacob Ruden and Kris Wehage during the building of the setup. Scanning electron microscopy was carried out in the Center for Microanalysis of Materials, University of Illinois, which is supported by the U.S. Department of Energy under Grant No. DEFG02-96ER-4539.

APPENDIX: DETERMINATION OF STRESSES

Using the equation of normal equilibrium

$$(\sigma_0+\sigma_r)\frac{dz}{dr}=-\frac{pr}{2h} \tag{A1}$$

(with σ_0: residual stress, σ_r: radial stress, r: radial coordinate with the origin at the center, and z: deflection of the membrane), along with Hooke's Law and strain-displacement relations, we get

$$\frac{1}{\rho}\left(\frac{\sigma_0+\sigma_r}{k}\right)^2\frac{d}{d\rho}\left(\frac{\sigma_r+\sigma_\theta}{k}\right)+8=0, \tag{A2}$$

where σ_θ is the tangential stress, and $\rho=r/a$ and $k=(E/4)(pa/Eh)^{2/3}$.

Due to the symmetry of the problem, the following series solution is assumed for σ_r:

$$\sigma_0+\sigma_r=k(B_0+B_2\rho^2+B_4\rho^4+\cdots). \tag{A3}$$

Substituting this into the radial equation of equilibrium:

$$\sigma_\theta=\frac{d}{dr}(r\sigma_r), \tag{A4}$$

we find

$$\sigma_0+\sigma_\theta=k(B_0+3B_2\rho^2+5B_4\rho^4+\cdots). \tag{A5}$$

Substituting both series of Eqs. (A3) and (A5) in Eq. (A2) gives

$$(B_0+B_2\rho^2+B_4\rho^4+\cdots)^2(B_2+3B_4\rho^2+6B_6\rho^4+10B_8\rho^6+\cdots)+1=0. \tag{A6}$$

After expanding the product of Eq. (A6) and equating coefficients to zero, B_i can be expressed as a function of B_0:

$$B_2 = -\frac{1}{B_0^2},$$

$$B_4 = -\frac{2}{3B_0^5}, \tag{A7}$$

$$B_6 = -\frac{13}{18B_0^8},$$

etc.

The next step is the determination of B_0. It is realized by considering the clamped boundary condition at the edge, i.e., $\sigma_\theta - \nu\sigma_r = 0$ at $r = a$. This can be expressed in the following form:

$$(1-\nu)B_0 + (3-\nu)B_2 + (5-\nu)B_4 + \cdots = (1-\nu)\sigma_0/k. \tag{A8}$$

For a chosen Poisson's ratio, B_0 can be calculated from Eq. (A8) by substituting the relations of Eq. (A7).

Finally, from Eq. (A3) or (A5) the equibiaxial stress state σ at the midpoint, i.e., $r = 0$, can be expressed as

$$\frac{\sigma}{k} = B_0 - \frac{\sigma_0}{k}. \tag{A9}$$

[1] R. C. Cammarata, J. C. Bilello, A. L. Greer, K. Sieradzki, and S. M. Yalisove, MRS Bull. **24**, 34 (1999).
[2] C. V. Thompson and R. Carel, J. Mech. Phys. Solids **44**, 657 (1996).
[3] F. Spaepen, Acta Mater. **48**, 31 (2000).
[4] W. N. Sharpe, Jr., B. Yuan, and R. L. Edwards, IEEE J. Microelectromech. Syst. **6**, 193 (1997).
[5] V. M. Paviot, J. J. Vlassak, and W. D. Nix, Mater. Res. Soc. Symp. Proc. **356**, 579 (1995).
[6] H. H. Stevens, Jr., Exp. Stress Anal. **2**, 139 (1944).
[7] I. L. Hopkins, W. O. Baker, and J. B. Howard, J. Appl. Phys. **21**, 206 (1950).
[8] K. Haas and P. H. Geil, J. Polym. Sci., Part A-2 **4**, 289 (1966).
[9] R. P. Vinci and J. J. Vlassak, Annu. Rev. Mater. Sci. **26**, 431 (1996).
[10] J. J. Vlassak and W. D. Nix, J. Mech. Phys. Solids **42**, 1223 (1994).
[11] J. A. Lin and W. N. Unertl, J. Adhes. Sci. Technol. **8**, 913 (1994).
[12] A. G. Evans and J. W. Hutchinson, Acta Metall. Mater. **43**, 2507 (1995).
[13] J. Koike, S. Utsunomiya, Y. Shimoyama, K. Maruyama, and H. Oikawa, J. Mater. Res. **13**, 3256 (1998).
[14] R. Schwaiger and O. Kraft, Scr. Mater. **41**, 823 (1999).
[15] Y. Higo, K. Takashima, M. Shimojo, S. Sugiura, B. Pfister, and M. V. Swain, Mater. Res. Soc. Symp. Proc. **605**, 241 (2000).
[16] M. T. A. Saif, B. E. Alaca, and H. Sehitoglu, IEEE J. Microelectromech. Syst. **8**, 335 (1999).
[17] J. W. Hutchinson and Z. Suo, Adv. Appl. Mech. **29**, 63 (1992).
[18] J. L. Beuth, Jr., Int. J. Solids Struct. **29**, 1657 (1992).
[19] Z. C. Xia and J. W. Hutchinson, J. Mech. Phys. Solids **48**, 1107 (2000).
[20] W. Kern, RCA Eng. **28**, 99 (1983).
[21] A. A. Ayón, R. Braff, C. C. Lin, H. H. Sawin, and M. A. Schmidt, J. Electrochem. Soc. **146**, 339 (1999).
[22] F. Laermer, A. Schilp, K. Funk, and M. Offenberg, Proceedings of the 1999 12th IEEE International Conference on Micro Electro Mechanical Systems, MEMS, Orlando, FL, 17–21 January (1999), p. 211.
[23] M. G. Allen and S. D. Senturia, J. Adhes. **25**, 303 (1988).
[24] F. Maseeh and S. D. Senturia, in *Polyimides: Materials, Chemistry, and Characterization, Proceedings of the Third International Conference on Polyimides. Ellenville, New York. 2–4 November 1988*, edited by C. Feger, M. M. Khojasteh, and J. E. McGrath (Elsevier Science, Amsterdam, 1989), p. 575.
[25] H. Hencky, Z. Math. Phys. **63**, 311 (1915).
[26] W. B. Fichter, NASA TP-3658 (1997).
[27] J. D. Campbell, Q. J. Mech. Appl. Math. **9**, 84 (1956).
[28] K. Nakasa, S. Takata, and H. Ichigo, Eng. Fract. Mech. **59**, 191 (1998).
[29] A. Groisman and E. Kaplan, Europhys. Lett. **25**, 415 (1994).
[30] G. Müller, J. Geophys. Res. **103**, 15239 (1998).
[31] A. Aydin and J. M. DeGraff, Science **239**, 471 (1988).
[32] J. T. Neal, A. M. Langer, and P. F. Kerr, Geol. Soc. Am. Bull. **79**, 69 (1968).
[33] R. Weinberger, J. Struct. Geol. **21**, 379 (1999).
[34] J.-M. Konrad and R. Ayad, Can. Geotech. J. **34**, 929 (1997).